Available online at www.sciencedirect.com
SCIENCE DIRECT®
International Journal of Heat and Mass Transfer 48 (2005) 265–278
International Journal of HEAT and MASS TRANSFER
www.elsevier.com/locate/ijhmt

Effects of the liquid polarity and the wall slip on the heat and mass transport characteristics of the micro-scale evaporating transition film

Sang-Kwon Wee [a,1], Kenneth D. Kihm [a,*], Kevin P. Hallinan [b]

[a] Department of Mechanical, Aerospace and Biomedical Engineering, University of Tennessee, Knoxville, TN 37996, USA
[b] Department of Mechanical and Aerospace Engineering, University of Dayton, Dayton, OH 45469, USA

Received 12 March 2004; received in revised form 23 August 2004

Abstract

A mathematical model is developed to describe the micro-/nano-scale fluid flow and heat/mass transfer phenomena in an evaporating extended meniscus, focusing on the transition film region under non-isothermal interfacial conditions. The model incorporates polarity contributions to the working fluid field, a slip boundary condition on the solid wall, and thermocapillary stresses at the liquid–vapor interface. Two different disjoining pressure models, one polar and one non-polar, are considered for water as the working fluid so that the effect of polar interactions between the working fluid and solid surface can be exclusively examined on heat and mass transfer from the thin film. The polar effect is examined for the thin film established in a 20-μm diameter capillary pore. The effect of the slip boundary condition is separately examined for the thin film developed in a two-dimensional 20-μm slotted pore. The analytical results show that for a polar liquid, the transition region of the evaporating meniscus is longer than that of a non-polar liquid. In addition, the strong polar attraction with the solid wall acts to lower the evaporative heat transfer flux. The slip boundary condition, on the other hand, increases evaporative heat and mass flux and lowers the liquid pressure gradients and viscous drag at the wall. The slip effect shows a more pronounced enhancement as superheat increases. Another thing to note is that the slip effect of elongating the transition region can counteract the thermocapillary action of reducing the region and a potential delay of thermocapillary driven instability onset may be anticipated.

Keywords: Thin film evaporation; Thermocapillary; Micro-/nano-scale; Slip effect; Polarity effect

1. Introduction

Recently phase change heat transport devices such as heat pipes, capillary pumped loops and grooved evaporators have received much attention for their promise to dissipate large heat fluxes and to maintain temperature uniformity [1]. Many of these devices make use of thin film evaporation which takes place on the liquid–vapor interface of heated meniscus. Thin film evaporation is

* Corresponding author. Tel.: +1 865 974 5292; fax: +1 865 974 5274.
E-mail address: kkihm@utk.edu (K.D. Kihm).
[1] Currently at Digital Research Center, Samsung Advanced Institute of Technology, Suwon 440-600, Korea.

0017-9310/$ - see front matter © 2004 Elsevier Ltd. All rights reserved.
doi:10.1016/j.ijheatmasstransfer.2004.08.021

Nomenclature

a	coefficient for evaporative mass flux
A	dispersion constant, J
$6\pi A$	Hamaker constant, J
A_1	coefficient for slip length
B_1	coefficient for slip length
b	coefficient for evaporative mass flux
C	accommodation constant
h	thin film thickness, m
h_{fg}	latent heat of vaporization, J/kg
k	thermal conductivity, W/(m K)
K	curvature of liquid–vapor interface, 1/m
L_s	slip length, m
$\dot{m}_{evp}$	evaporative mass flux, kg/(m^2 s)
M	molecular weight, kg/kmol
P	pressure, Pa
q	heat flux, W/m^2
Q	total heat transfer rate, W
r	radial coordinate normal to substrate, m
R	pore radius, m
$\overline{R}$	universal gas constant, J/(kg K)
R_g	gas constant, J/(kg K)
T	temperature, K
u	velocity component in x-direction, m/s
v	vapor phase
w	wall
u^*	characteristic axial velocity, m/s
V_1	molar volume, m^3/mol
x	axial coordinate parallel to substrate, m

Greek symbols

α	coefficient for disjoining pressure
β	coefficient for disjoining pressure
Γ	mass flow rate, kg/s
γ	slope of surface tension, N/(m K)
$\dot{\gamma}$	shear rate, 1/s
μ	dynamic viscosity, N s/m^2
ν	kinematic viscosity, m^2/s
η	dimensionless film thickness
θ	dimensionless temperature
τ	shear stress, N/m^2
ρ	density, kg/m^3
ξ	dimensionless axial coordinate
Π	disjoining pressure, Pa
σ	surface tension, N/m

Subscripts

0	adsorbed film region
c	critical value
i	liquid–vapor interface
l	liquid phase
tr	transition

also of major importance in nucleate boiling heat transfer [2].

In phase change transport devices, capillary forces drive overall circulation of working fluid from an evaporator section to a condenser section, whereas the thin film flows at the evaporating meniscus are driven by capillarity and disjoining pressure gradient. Fig. 1 shows an evaporating extended meniscus developed on the wall within a capillary pore. The extended meniscus is composed of three distinct regions [3]. The bulk meniscus region is dominated by capillary forces, while the adsorbed film region is governed by the disjoining pressure due to intermolecular interactions between the wall and the fluid. In the adsorbed film, superheated liquid molecules are restrained from evaporation by extremely strong interaction forces between the liquid molecules and the

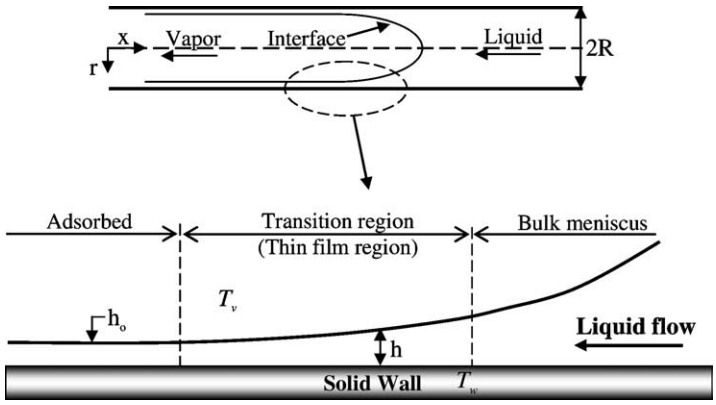

Fig. 1. Schematic of liquid–vapor interface forming within a cylindrical capillary pore with uniform wall temperature.

solid substrate. The thin film region, which is called a transition region, exists between the bulk meniscus and the adsorbed film region. The effect of capillarity and disjoining pressure are equally important in this region for fluid flow and heat transfer.

The foundation for the study of fluid mechanics and thermodynamics of thin liquid film was established by Derjaguin et al. [4]. They proposed the concept of a disjoining pressure for representing the influence of interaction between substrate and fluid on the pressure field in a thin film. The disjoining pressure has been included in the liquid pressure gradient for the analysis of evaporation of liquid film. Studies on evaporating extended meniscus have been extensively done by many researchers as summarized in Table 1.

Potash and Wayner [3] used this disjoining pressure concept to describe evaporation from a steady state, two-dimensional, extended meniscus on a heated vertical flat plate immersed in a liquid. They were the first to show that the pressure gradient and evaporative mass flux reached a maximum in an evaporating thin film region. Wayner et al. [5] examined evaporation from a stable extended meniscus formed on an inclined flat plate for non-polar liquids. In this work they demonstrated that the heat transfer coefficient increased rapidly from zero at the adsorbed film to a constant value at the end of transition region over a very short distance. Moosman and Homsy [6] developed a mathematical model to describe the transition phenomena in the horizontal extended meniscus using perturbation analysis. Their analysis showed that the maximum heat flux and evaporation flux occurred in the transition region where the thermal resistance was small. These three pioneering studies [4–6] considered the non-isothermal interfacial conditions but without incorporating thermocapillary effect in details.

Mirzamoghadam and Catton [7] developed an analytical model of an evaporating meniscus developing on an inclined heated copper plate submerged in a non-polar liquid pool at various angles. They showed that the heat and mass transport were dependent on angle of inclination of the plate and an angle of 20–30° yielded an increase in the heat transfer coefficient by a factor of seven compared to a horizontal case. Stephan and Busse [8] uniquely calculated the heat and mass transport phenomena in both the thin film region and the macroscopic meniscus within a heat pipe with open grooves. They found that the heat transfer in the thin film region could have a significant influence on the overall macroscopic heat transfer. Swanson and Herdt [9] investigated the fluid flow and heat transfer in a three-dimensional capillary pore geometry by incorporating Marangoni convection, London–van der Waals dispersion forces, and non-isothermal interface conditions. They assumed a Hagen–Poiseuille flow field for the liquid in the meniscus and thin film regions and obtained the change in the meniscus shape with varying dispersion number. They showed that the local evaporative mass flux increased dramatically as the dispersion number was increased. These three studies [7–9] incorporated the thermocapillary effect associated with the non-isothermal interface, but were limited to non-polar liquids such as pentane.

Hallinan et al. [10] developed a model to describe the evaporation thin film within micropores of porous wick structure of heat pipe under non-isothermal condition and thus accounted for thermocapillary stresses at the interface. They also found that maximum evaporative fluxes were present in the extended meniscus with constant wall temperature. Recently, Park et al. [11] developed a mathematical model to describe the transport phenomena for a thin film region of a micro-channel with a non-polar liquid under isothermal conditions. They showed that the gradient in the vapor pressure had a significant influence on the thin film profile. They also found that the length and the maximum thickness of the thin film decreased exponentially as the heat flux increased.

Table 1
Comparison of previous studies on evaporating extended meniscus

Authors	Non-isothermal interfacial condition	Thermocapillary effect	Slip boundary condition	Polarity effect
Potash and Wayner [3]	O	X	X	X
Wayner et al. [5]	O	X	X	X
Moosman and Homsy [6]	O	X	X	X
Mirzamoghadam and Catton [7]	O	O	X	X
Stephan and Busse [8]	O	O	X	X
Swanson and Herdt [9]	O	O	X	X
Hallinan et al. [10]	O	X	X	X
Park et al. [11]	X	X	O	X
Qu and Ma [15]	O	X	X	O
Wee et al., present study	O	O	O	O

O: included in the analysis; X: not included in the analysis.

In general the working fluids used in the phase change heat transport devices are classified into two groups: non-polar and polar liquids. Pentane, decane, heptane, carbon tetrachloride belong to the non-polar liquid group, and water, ammonia, acetone, ethanol, and methanol are in the polar liquid group. As stated above, most of the liquids that have been used in the study of liquid–vapor phase change transport are non-polar liquids [4–11]. For these liquids, the primary cause of the disjoining pressure is London dispersion forces resulting from the interaction of the positive nucleus of one molecule with the electrons of another molecule. The dispersion forces are the weakest of the van der Waals forces. Therefore, the intermolecular forces for non-polar molecules are weak for restraining the liquid molecules from evaporation and thus the evaporation rates are large. However, dispersion forces provide the most important contribution to the total van der Waals force between atoms and molecules because they are always present in non-polar and polar molecules as well. On the other hand, for polar liquids other interaction forces, such as dipole–dipole interactions are present. The positive charge of one molecule attracts the negative charge of another molecule [12]. For a water molecule, negative charges around oxygen molecules attract the positively charged hydrogen molecule, which leads to strong dipole moment [13]. These forces are stronger and longer ranged than dispersion forces. Since polar fluid molecules yield much stronger intermolecular forces with a solid substrate, the evaporation rate of polar liquid tends to be lower relative to non-polar liquid [14].

Most research of evaporating thin films has considered only non-polar liquids. Recently, Qu and Ma [15] studied the polarity effects of different working fluids on the evaporation heat transfer characteristics from a meniscus in a capillary tube. They noted that the disjoining pressure had strong effects on liquid film thickness profiles and the effects were more dominant in strongly polar working fluid such as water. They found that the strong disjoining pressure in a polar liquid leads to elongation of the evaporating interfacial region relative to that of non-polar liquids such as carbon tetrachloride and benzene. Their study, however, did not include the thermocapillary effect though non-isothermal interfacial conditions were incorporated.

With the proliferation of MEMS and nano-technology, flow phenomena have been studied at smaller scales. At the micro-/nano-scale, flow cannot always be modeled based on a continuum hypothesis. The deviation of the gas flow from the continuum hypothesis is measured by the Knudsen number, which is defined as the ratio of the mean free path to the characteristic length scale. For liquids, however, the concept of the mean free path is not useful so that the Knudsen number cannot be defined. More relevant to liquids at the micro-scale is slip at the wall [16]. Several researchers have recently demonstrated that the no-slip boundary condition may not be applicable to both the micro- and nano-scale liquid flow. Ruckenstein and Dunn [17] established a model for a slip velocity at the contact line region of a spreading liquid drop on a solid surface. They noted that a gradient of chemical potential along the interface of liquid and solid induces a force which causes the slip. Neogi and Miller [18] calculated spreading of an axisymmetric sessile drop over a solid medium using a slip condition which was equal to the slip velocity of Ruckenstein and Dunn [17]. They demonstrated that intermolecular forces in the contact line region had an effect on the surface diffusion of adsorbed molecules which produced slip on a wall substrate. Ruckenstein and Rajora [19] compared the slip velocity modeled by a chemical potential theory with the slip velocity measured experimentally in a sufficiently small capillary. They determined the slip velocity with the use of the chemical potential theory, where the slip velocity was proportional to a gradient in the chemical potential caused by pressure drop in capillary pore. They demonstrated that the slip velocity was related to surface diffusion coefficients and the pressure gradient. Recently, Thompson and Troian [20] provided molecular dynamic (MD) simulations to quantify the slip-flow boundary conditions in liquid flows. Based on their results, they suggested a more general boundary condition for liquid flow at a solid–liquid interface. Choi et al. [21] examined the slip effects of water flow in hydrophilic and hydrophobic micro-channels experimentally. They concluded that the effect of the slip velocity yielded greater flow rates than predicted using a no-slip boundary condition. From their experimental results, they obtained a relationship between the shear rate and slip length that had the same form as that of Thompson and Troian [20], but with different coefficients. Tretheway and Meinhart [22] measured the velocity profile in hydrophobic micro-channel using micro-particle image velocimetry. In their experiments, they measured an apparent slip velocity which was about 10% of free stream velocity and a slip length of approximately 1 μm. They concluded that the no-slip condition could be inaccurate for micro-scale fluid flow modeling.

While all the above mentioned studies [16–22] considered only hydrodynamic aspects of slip boundary conditions, the only published study accounting for an evaporating thin film is presented by Park et al. [11]. They applied the slip velocity conditions to an evaporating micro-channel filled with water under very simplified conditions. Thermocapillary effects were not considered. Nevertheless, they concluded that the slip velocity boundary condition had a significance influence on the fluid and heat transport processes.

The slip boundary condition is related to the pressure gradient that gives rise to the flowfield of an evaporating meniscus within capillary driven heat transport. Such

devices rely upon large pressure gradients in the thin film region to sustain the evaporation. A larger evaporative flow, and therefore thin film pressure gradient, yields an increased slip velocity. Therefore, recently developed thermal control devices having high thermal performance and thus large liquid pressure gradients in thin films can only be accurately modeled by considering a slip velocity condition near the contact line. As the characteristic length of a pore or groove decreases, the slip effects become more important. Further, the slip velocity becomes more important with increase in heat flux in thin film transition region, as will be shown in detail later. According to several experimental investigations, the film thickness in the transition region has been measured to be on the order of tens to hundreds of nanometers [23]. Given slip lengths on the order of micron, slip cannot be ignored when modeling the thermofluid characteristics of an evaporating thin film.

Finally temperature gradients along an evaporating meniscus generate surface tension gradients, which in turn induce the thermocapillary stresses that seek to drive fluid flow away from the adsorbed region to meniscus region. This thremocapillary stress can result in Marangoni convection within the transition region. This flow is increased as the heat flux increases. At a certain critical value of heat flux, instabilities arise due to the thermocapillary effects [24]. Since polar liquids have larger surface tensions and surface tension slope with temperature, it is even more important to include thermocapillary contributions to the thermofluid characteristics.

Although extensive research of an evaporating non-polar thin films has been performed due to the simplicity of modeling van der Waals intermolecular forces, a complete understanding has not been achieved yet. In this study we utilize a more complete model of an evaporating extended meniscus formed in a heated capillary pore than in reported research to date. Here, an extended study is conducted to examine the effect of polar interactions between fluid and substrate by considering water as the working fluid wherein a virtual non-polar model is imposed for the study and the results are compared with those with a practical polar model to exclusively examine the polarity effect. The model developed in a cylindrical coordinate system also incorporates thermocapillary stresses due to non-isothermal conditions. It also accounts for slip at the wall. This latter influence is evaluated for a non-polar liquid such as pentane and a slightly polar liquid such as ammonia in a slotted pore, in order to alleviate the computational complexity associated with cylindrical coordinates. As summarized in Table 1, the present study will be the first attempt to comprehensively incorporate the non-isothermal interface associated with thermocapillary stresses, slip boundary conditions, and polar fluid–substrate interactions.

2. Mathematical modeling of an evaporating extended meniscus

2.1. Modeling for disjoining pressure and thin film geometry

A mathematical model of an evaporating liquid thin film in steady state is considered for a circular pore geometry as is illustrated in Fig. 1. The liquid is assumed to be heated by a uniform heat flux from a solid substrate causing evaporation from the liquid–vapor interface. It is assumed that the evaporative flow from the thin film is sustained by constant liquid inflow from the bulk meniscus controlled by gradients in capillary and disjoining pressure. The origin is set at the junction of the non-evaporating adsorbed film region and the evaporating transition region.

The pressure differential is related to capillary pressure and disjoining pressure in augmented Laplace–Young equation given as

$$P_v - P_l = \sigma K + \Pi \tag{1}$$

where P_v and P_l are the pressure of the vapor and liquid phases, respectively, Π is the disjoining pressure, which represents the intermolecular interaction force between the liquid and solid molecules present in the thin liquid film, σ is a liquid–vapor interfacial surface tension, and K is a mean curvature of liquid–vapor interface. The surface tension is related to the local liquid–vapor interfacial temperature using a linear approximation by

$$\sigma = \sigma_0 + \gamma T_i \tag{2}$$

where σ_0 is the reference surface tension, γ is the surface tension–temperature slope (typically <0), and T_i is the interface temperature, respectively. The mean curvature for circular pores is expressed as the sum of the circumferential curvature and axial curvature which are represented in terms of the first and second derivative of the film thickness with the distance along the substrate:

$$K = \left(\frac{1}{R-h}\right)(1+h_x^2)^{-0.5} + h_{xx}(1+h_x^2)^{-1.5} \tag{3}$$

The subscript x indicates the derivative with respect to x and R is the radius of circular pore.

Both polar and non-polar forms of the disjoining pressure are utilized so as to comparatively ascertain the role of polar forces on the thin film thermofluid characteristics. For a polar liquid like water the disjoining pressure has been characterized for a two-dimensional extended meniscus [3] by the equation,

$$\Pi = -\rho_l R_g T_i \ln(P_{v,i}/P^0_{v,i}) \tag{4}$$

where ρ_l is the density of the liquid phase, R_g is the gas constant, T_i is the liquid–vapor interface temperature, $P_{v,i}$ is the reduced saturation pressure of the film, and $P^0_{v,i}$ is the saturation pressure corresponding to T_i.

Combining the experimental work of Derjaguin and Zorin [25] with Eq. (4), Holm and Goplen [26] developed the expression of the disjoining pressure as a logarithmic function of film thickness in the following form:

$$\Pi = -\rho_l R_g T_i \ln(\alpha h(x)^{\beta}) \tag{5}$$

For pure water on the quartz glass, the constants are given as $\alpha = 1.49$, $\beta = 0.0243$ [26]. On the other hand, the disjoining pressure for non-polar liquids is expressed in the polynomial function of the film thickness in the non-retarded form [25]

$$\Pi = \frac{A}{h^3} \tag{6}$$

where $6\pi A$ is the Hamakar constant, which is positive for a completely wetting liquid, and A is the dispersion constant equal to 3.11×10^{-21} J for water [5].

2.2. Modeling for liquid flow field and slip boundary condition

The fluid dynamics can be modeled with the lubrication approximation yielding in cylindrical coordinate:

$$\frac{1}{r}\frac{\partial}{\partial r}\left(r\frac{\partial u}{\partial r}\right) = \frac{1}{\mu_l}\frac{dP_l}{dx} \tag{7}$$

The solution to the above differential equation is subject to the following boundary conditions at the solid wall and liquid–vapor interface, respectively:

$$\text{at } r = R, \quad u = u_s = -L_s \left.\frac{du}{dr}\right|_{wall} \tag{8}$$

$$\text{at } r = R - h, \quad -\mu\frac{\partial u}{\partial r} = \frac{d\sigma}{dx} \tag{9}$$

The first boundary condition, Eq. (8), is the slip boundary condition at wall, which was proposed by Navier [27] to incorporate the possibility of flow slip. L_s is the slip length that is an imaginary length from the wall at which the velocity extrapolates to zero. If L_s is zero, this is identical to a no-slip condition. Thompson and Troian [20] proposed the following relationship of slip length to shear rate:

$$L_s = L_{s0}(1 - \dot{\gamma}/\dot{\gamma}_c)^{-1/2} \tag{10}$$

This relation was achieved in the numerical study of a micro-Couette flow by the use of molecular dynamics simulations. A similar form of the relation was obtained experimentally by Choi et al. [21] in hydrophobic and hydrophilic micro-channels with water as shown:

$$L_s = A_1 \dot{\gamma}^{B_1} \tag{11}$$

where $\dot{\gamma}$ is the shear rate at the wall and the coefficients, A_1 and B_1, are experiment dependent. In this study, using the correlation of Thompson and Troian [20] the slip effect on the micro-scale heat and mass transfer is investigated for working fluids of pentane and ammonia.

The second boundary condition, Eq. (9), is the shear stress condition at the liquid–vapor interface, which equates the interfacial shear stress to the change in surface tension. The surface tension gradient is caused by temperature gradients at the interface.

The liquid velocity profile can now be determined by solving the axial momentum equation, Eq. (7), subject to the specified boundary conditions,

$$u(r) = \frac{1}{4\mu_l}\frac{dP_l}{dx}r^2 + C_1 \ln r + C_2 \tag{12}$$

where

$$C_1 = -\frac{1}{\mu_l}\frac{d\sigma}{dx}(R-h) - \frac{1}{2\mu_l}\frac{dP_l}{dx}(R-h)^2 \tag{13}$$

and

$$C_2 = -L_s\left(\frac{1}{2\mu_l}\frac{dP_l}{dx}R + \frac{C_1}{R}\right) - \frac{1}{4\mu_l}\frac{dP_l}{dx}R^2 - C_1 \ln R. \tag{14}$$

The slip velocity, $u_s = u(r = R)$, can be related to C_1 and C_2 as follows and it clearly depends upon the local pressure gradient.

$$u_s = \frac{1}{4\mu_l}\frac{dP_l}{dx}R^2 + C_1 \ln R + C_2. \tag{15}$$

Using the velocity profile given by Eq. (12), the mass flow rate across a cross-sectional area of the film thickness h is obtained as follows:

$$\Gamma = \int_{R-h}^{R} \rho_l \left[\frac{1}{4\mu_l}\frac{dP_l}{dx}r^2 + C_1 \ln r + C_2\right] 2\pi r\, dr. \tag{16}$$

After integration, the following expression is derived:

$$\Gamma = C_6\frac{dP_l}{dx} + C_7\frac{d\sigma}{dx} \tag{17}$$

where

$$C_6 = \frac{\pi}{8\nu_l}\left\{[R^4 - (R-h)^4] - 4(R-h)^2 C_5\right\} + \pi\rho_l(2Rh - h^2)C_3, \tag{18}$$

$$C_7 = -\frac{\pi}{\nu_l}(R-h)C_5 + \pi\rho_l(2Rh - h^2)C_4 \tag{19}$$

The coefficients C_3, C_4, and C_5 are defined as follows:

$$C_3 = \frac{L_s}{2\mu_l}\left[\frac{(R-h)^2}{R} - R\right] + \frac{1}{2\mu_l}\left[(R-h)^2 \ln R - \frac{1}{2}R^2\right], \tag{20}$$

$$C_4 = \frac{L_s}{\mu_l}\frac{(R-h)}{R} + \frac{1}{\mu_l}(R-h)\ln R \tag{21}$$

and

$$C_5 = R^2\left(\ln R - \frac{1}{2}\right) - (R-h)^2\left[\ln(R-h) - \frac{1}{2}\right]. \tag{22}$$

These coefficients are related to R, h, μ_l, and ρ_l. Fluid slip at the wall is incorporated in the terms which include the slip length (L_s) (Eqs. (20) and (21)).

The evaporative mass flux is related to the mass flow rate in the thin film through mass conservation,

$$\frac{d\Gamma}{dx} = -\dot{m}_{evp}. \tag{23}$$

Using kinetic theory to relate the net mass flux of matter crossing a liquid–vapor interface to a jump change in interfacial temperature at the interface [28] and an extended Clapeyron equation to equate the variation in the equilibrium vapor pressure with temperature and disjoining pressure, the evaporating mass flux, $\dot{m}_{evp}$, is modeled as a function of the temperature and pressure jumps at the interface [29]:

$$\dot{m}_{evp} = a(T_i - T_v) + b(P_l - P_v) \tag{24}$$

The coefficients, a and b, are dependent on the physical properties of the liquid and defined as follows:

$$\begin{aligned} a &= C\left(\frac{M}{2\pi\overline{R}T_i}\right)^{1/2}\left(\frac{P_v M h_{fg}}{\overline{R}T_v T_i}\right), \\ b &= C\left(\frac{M}{2\pi\overline{R}T_i}\right)^{1/2}\left(\frac{V_l P_v}{\overline{R}T_i}\right) \end{aligned} \tag{25}$$

where, C is the accommodation coefficient, taken to be 2.0, M is the liquid molecular weight, $\overline{R}$ is the universal gas constant, P_v is the saturated vapor pressure of liquid at temperature T_v, V_l is the liquid molar volume at temperature T_i and h_{fg} is the latent heat of vaporization per unit mass at T_i. The vapor phase is assumed to have a uniform pressure and temperature. Eq. (24) shows that the local evaporation rate is a function of the local superheat and the liquid pressure, which is influenced by both capillary and disjoining pressure. The liquid–vapor interfacial temperature varies with the film thickness, as changes in film thickness are associated with changes in the conduction resistance. The vapor phase is assumed to be isothermal and pure.

2.3. Modeling for thermal field and heat transfer

The liquid–vapor interface temperature can be obtained using the steady-state energy equation. The thickness of the liquid film is so small that the conduction heat transfer through the liquid thin film is assumed to be present only the direction perpendicular to the solid surface. According to Stephan and Busse [8], the calculated normal temperature gradients are several orders of magnitude larger than the gradients parallel to the surface. Also, the conduction heat transfer rate from the wall through the liquid film to the liquid–vapor interface balances to both of evaporation and convection at the interface [6]. Of these two, evaporative losses are dominant. Thus, the conduction heat transfer rate is set equal to the evaporation heat flux at the interface. This yields the following simplified energy equation in cylindrical coordinates:

$$\frac{\partial}{\partial r}\left(k_l r \frac{\partial T}{\partial r}\right) = 0 \tag{26}$$

Two boundary conditions are necessary at wall and liquid–vapor interface for obtaining the temperature distribution:

$$\text{at } r = R, \quad T = T_w \tag{27}$$

$$\text{at } r = R - h, \quad k_l \left.\frac{dT}{dr}\right|_{r=R-h} = \dot{m}_{evp} h_{fg} \tag{28}$$

These correspond to a specified wall temperature and a balance between conduction and evaporation heat transfer at the liquid–vapor interface, respectively. Solution of the energy equation, Eq. (26), subject to these boundary conditions gives the temperature variation along the interface

$$T_i = -\frac{h_{fg}}{k_l}(R-h)\ln\left(\frac{R}{R-h}\right)\dot{m}_{evp} + T_w \tag{29}$$

The evaporation mass flux given by Eq. (24) is substituted into Eq. (29) and using the definitions for the disjoining pressure and capillary force to relate P_v in Eq. (24) to P_l, the final expression for the interfacial temperature results in

$$T_i = \frac{T_w k_l/F_1 + aT_v + b\sigma K}{k_l/F_1 + a + b\rho_l R_g \ln(\alpha h^\beta)} \tag{30}$$

where

$$F_1 = (R-h)h_{fg}\ln\left(\frac{R}{R-h}\right) \tag{31}$$

2.4. Integrated modeling for combined flow and thermal fields

Integrating the evaporative mass flux from the adsorbed film to an arbitrary x-location, the mass flow rate can be related to the interfacial temperature and film thickness as shown:

$$\Gamma(x) = -\frac{2\pi k_l}{h_{fg}}\int_0^x \frac{T_w - T_i}{\ln\left(\frac{R}{R-h}\right)}\,dx \tag{32}$$

This expression for $\Gamma(x)$ provides closure to Eq. (17). The RHS of Eq. (17) must be equal to this expression for $\Gamma(x)$. In Eq. (17) the liquid pressure gradient can be obtained by differentiation of the augmented Laplace–Young equation, Eq. (1), in terms of x,

$$\frac{dP_l}{dx} = -\sigma\frac{dK}{dx} - K\frac{d\sigma}{dx} - \frac{d\Pi}{dx} \tag{33}$$

Eq. (33) shows that the thin film flow is controlled by gradients in curvature, surface tension, and disjoining pressure. Of these, only the disjoining pressure term drives flow into the thin film region. The third-order non-linear differential equation for the film thickness profile can be obtained by substituting the expression for curvature into Eq. (33) and rearranging

$$h_{xxx} - 3h_{xx}^2 h_x(1+h_x^2)^{-1} - h_{xx}h_x(R-h)^{-1} + h_x(1+h_x^2)(R-h)^{-2} + \frac{\gamma}{\sigma}\left[(1+h_x^2)(R-h)^{-1} + h_{xx}\right]\frac{dT}{dx} + \frac{1}{\sigma}(1+h_x^2)^{1.5}\left(\frac{dP_l}{dx} + \frac{d\Pi}{dx}\right) = 0 \tag{34}$$

The liquid pressure gradient in terms of x is achieved by equating Eqs. (17) and (32),

$$\frac{dP_l}{dx} = -\frac{C_7}{C_6}\frac{d\sigma}{dx} - \frac{2\pi k_l}{h_{fg}C_6}\int_0^x \frac{T_w - T_i}{\ln[R/(R-h)]}dx \tag{35}$$

In Eq. (34), the conservation of mass equation combined with the interfacial normal stress balance within the film reduced to a differential equation for the thin film thickness profile along the horizontal solid wall. In this equation, all of the related physical properties such as temperature, pressure, flow velocities and evaporative mass flux are represented in terms of the liquid film thickness, h, and its derivatives. The influence of polar solid–liquid intermolecular forces is imbedded in the disjoining pressure term in Eq. (34) and the slip velocity effect is imbedded in the constants C_6 and C_7 in the liquid pressure gradient, Eq. (35), through its contribution to the mass flow rate, Eq. (17).

The ordinary differential Eq. (34) can be solved using sixth-order Runge–Kutta–Fehlberg method. The third-order differential equation needs three initial conditions at the adsorbed region, $x = 0$. The adsorbed film thickness can be calculated by setting Eq. (24) of the evaporation mass flux to zero at $x = 0$ since there is no evaporation at adsorbed film. For a completely wetting film the slope approaches a very small value at adsorbed film region; thus first derivative of film thickness is zero. The second derivative of the thickness would be zero as well. But these initial conditions yield the trivial solution of a constant film thickness profile. In order to avoid these trivial solutions, a small perturbation can be applied to the thickness and the slope [5,10]. The solution of Eq. (34) is very sensitive to the specification of the initial condition for the first derivative of thickness especially as the superheat increases. An iterative technique is employed to guess the slope at $x = 0$ such that the solution converges to the appropriate curvature in the bulk meniscus region. Once the liquid film thickness profile $h(x)$ is obtained from Eq. (34), the other properties are readily determined since they are all functions of $h(x)$, such as temperature (Eq. (30)), pressure gradient (Eq. (35)), and the evaporative mass flux (Eq. (24)).

3. Results and discussion

The working fluid is chosen as water for investigation of polarity effect in a cylindrical capillary pore of 20-μm diameter. In order to consider the slip effect separately, non-polar pentane and slightly polar ammonia are chosen for working fluids in slotted pore geometry. The physical properties are obtained for water at working temperature of 373 K and for pentane and ammonia at 300 K (Table 2), and the corresponding vapor was assumed to be saturated. Note that $x = 0$ is set to the point of zero evaporation mass flux as the beginning of the transition region in all the presented results.

3.1. Effect of liquid polarity

Fig. 2 shows meniscus profiles for three superheat conditions of water with a non-polar form of the disjoining pressure imposed, i.e., from Eq. (34) coupled with Eq. (6). This artificial elimination of the polarity of water is devised to separately examine the polarity effect on the development of evaporating thin film and its heat/mass transport characteristics. The superheat, represented by the temperature differential between T_w and T_v, is specified by the boundary condition of Eq. (27). The length of thin film (transition region) decreases with increasing superheat and the adsorbed film thickness also decreases with an increase in superheat, as magnified by the inset profiles.

Fig. 3a shows liquid pressure gradient profiles calculated from Eq. (35) for different superheat conditions. The transition region, which is approximately equivalent

Table 2
Physical properties of water, pentane and ammonia [30]

Physical properties	Water (at 373 K)	Pentane (at 300 K)	Ammonia (at 300 K)
ρ_l (kg/m^3)	958	619	600
μ_l (N s/m^2)	2.817×10^{-4}	2.144×10^{-4}	1.293×10^{-4}
k_l (W/m K)	0.679	0.111	0.480
h_{fg} (kJ/kg)	2258	361	1187
σ (N/m)	$0.1162–1.477\times10^{-4}T$	$0.0484–1.102\times10^{-4}T$	$0.0860–2.182\times10^{-4}T$

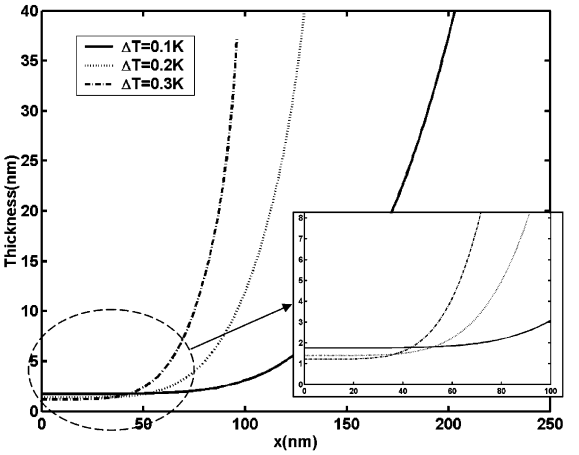

Fig. 2. Thin film profiles of water with non-polar disjoining pressure model imposed for three different superheat conditions accounting for thermocapillary effect.

to the range of non-zero pressure gradients, is clearly shown to decrease with increasing superheat. The maximum level of the pressure gradient increases with increasing superheat since a higher flow rate directed from the bulk to the thin film region is required to compensate the increased evaporation flux. Fig. 3b shows liquid pressure distribution for the same cases of Fig. 3a. While the liquid pressure in the bulk capillary region remains unchanged, the total pressure drop along the transition region increases with increasing superheat because of the higher compensating flow rate driven from the bulk region.

Fig. 4a shows the evaporative mass flux distributions calculated from Eq. (24) along the thin film per unit depth in meter for different superheat levels. The point of maximum evaporation mass flux exists within the thin film region for all superheat levels, and this has been persistently identified in the previous studies [5–11]. The location of the peak roughly corresponds to the location of the maximum pressure gradient shown in Fig. 3a. Fig. 4b shows the total evaporative mass flow rate integrated from the mass flux profiles in Fig. 4a. As expected, the total evaporative mass flux increases as the superheat increases.

Fig. 5 shows the change in the thin film profile for polar and non-polar liquids for the same superheat condition of 0.1 K. The length of the thin film or transition region, L_{tr}, is defined as the distance from the adsorbed region to the junction where the value of disjoining pressure is equal to that of capillary pressure. The length of transition region is calculated to 286 nm using a polar form of the disjoining pressure and to 96 nm for a non-polar form of the disjoining pressure. The polar form of the disjoining pressure extends the junction of pressure equality toward the bulk region, which in turn

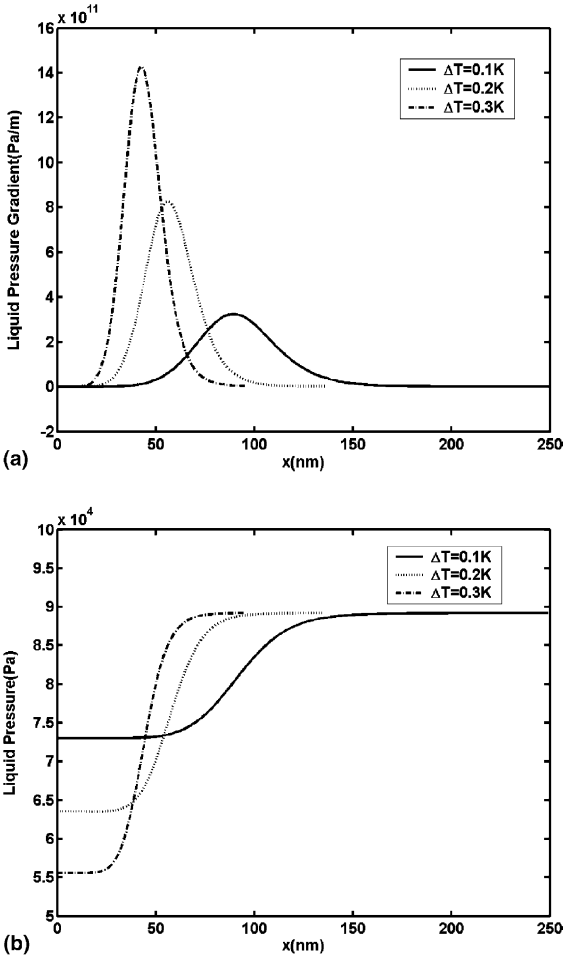

Fig. 3. Liquid pressure profiles in the transition region of non-polar water for different superheat conditions: (a) liquid pressure gradient calculated from Eq. (35); and (b) liquid pressure distribution integrated from (a).

results in the remarkable increase in L_{tr}. Also, the stronger attractive forces between the polar liquid and the solid substrate substantially increase the thin film thicknesses for the same superheat level. The elongation of the thin film region was similarly observed at high dispersion numbers, defined as the ratio of disjoining pressure to surface tension force, by Swanson and Herdt [9]. Qu and Ma [15] compared the meniscus profiles of water with those of other non-polar liquids, such as carbon tetrachloride and benzene, and also showed that the transition region of a polar liquid is much longer than that of a non-polar liquid under the same superheat condition.

Fig. 6 presents a comparison of disjoining pressure profiles for polar water (solid lines) and non-polar water (dashed lines) for the same superheat condition of 0.1 K. It is shown that the transition film length where the

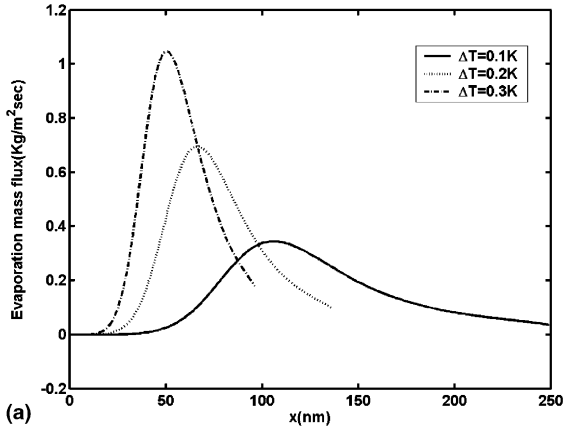

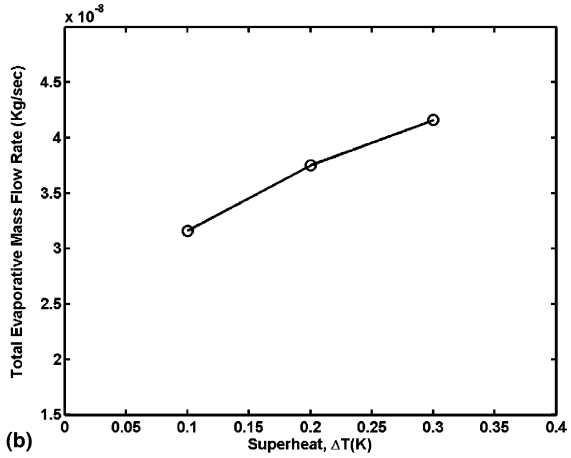

Fig. 4. Evaporative mass flux distribution in the transition region of non-polar water for different superheat conditions: (a) evaporative mass flux calculated from Eq. (24); and (b) total evaporative mass flow rate.

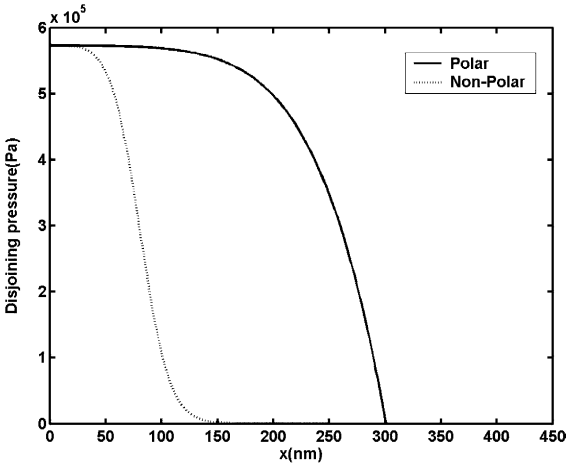

Fig. 6. Comparison of the disjoining pressure of non-polar water and polar water for the same superheat condition of $T_w - T_v = 0.1$ K.

disjoining pressure is significant is longer for the polar case due to its slower decrease of disjoining pressure, while the maximum value of the disjoining pressure remains the same for polar and non-polar water. The disjoining pressure of non-polar liquid gradually goes to zero based on Eq. (6), but that of polar liquid rather sharply drops to zero, reflecting the limitation of the disjoining pressure model for a polar liquid represented by Eq. (5). This deficiency later creates abrupt changes in the profiles of other physical parameters.

Fig. 7 shows that the evaporative mass flux for the non-polar case is larger than that of the polar case. The discontinuity shown in the evaporative mass flux distribution for a polar liquid is attributed to the aforementioned deficiency of the model used to describe the

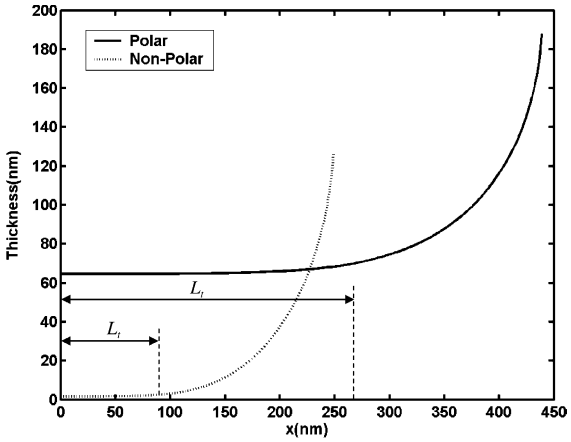

Fig. 5. Comparison of the thin film profiles of non-polar water and polar water for the same superheat condition of $T_w - T_v = 0.1$ K.

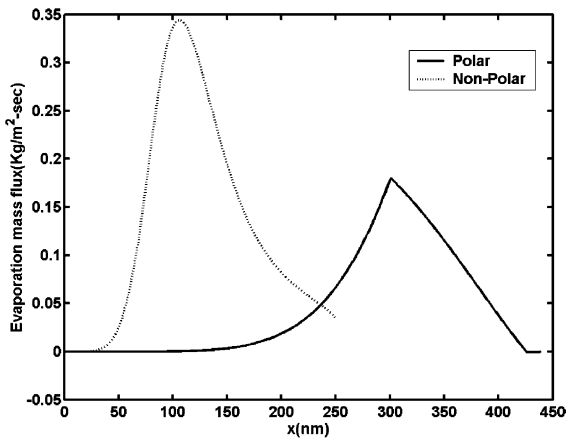

Fig. 7. Comparison of the evaporative mass flux of non-polar water and polar water for the same superheat condition of $T_w - T_v = 0.1$ K.

disjoining pressure for polar liquids. The average evaporative mass flux per unit axial length of the thin film region, for a unit width of 1-m, is calculated to 0.155 kg/(ms) for a non-polar liquid and 0.027 kg/(ms) for a polar liquid. The associated evaporative heat transport rate in the transition region is 35 W/cm^2 for a non-polar and 6 W/cm^2 for a polar liquid. As stated previously, the strong intermolecular forces retard the evaporation of liquid molecules from liquid–vapor interface in polar liquid.

3.2. Effect of liquid slip

The effect of inclusion of the slip boundary condition is investigated for pentane and ammonia in a two-dimensional slotted pore with 20-μm width. Pentane is chosen as non-polar liquid and ammonia as a slightly polar liquid. The differential equation for the film profile was obtained in non-dimensional form using following non-dimensional variables [10]:

$$\eta = \frac{h}{h_0}, \quad \xi = \frac{x}{x_0}, \quad \dot{m}_{id} = \rho_l u_0, \quad Ca = \frac{\mu_l u_0}{\sigma_0},$$
$$x_0 = \left(\frac{\sigma_0 h_0}{\Pi_0}\right)^{1/2}, \quad \theta = \frac{T_i - T_v}{T_w - T_v}, \quad \kappa = \frac{h_{fg}\dot{m}_{id}}{(k/h_0)},$$
$$\Delta T_0 = T_w - T_v, \quad \dot{m}_{id} = C\left(\frac{M}{2\pi \bar{R} T}\right)^{1/2}\left[\frac{P_v M h_{fg}}{\bar{R} T_v T_i}(T_i - T_v)\right]$$

where η and ξ are dimensionless film thickness and dimensionless axial coordinate, respectively, subscript '0' represents adsorbed film region, u_0 is a characteristics velocity of the liquid, Ca is capillary number, θ is non-dimensional temperature, and κ is the ratio of evaporative interfacial resistant to conductive resistant in thin film. Using these non-dimensional variables, the differential equation for non-dimensional film thickness profile was achieved by substituting Eq. (17) for mass flow rate (Γ) and Eq. (24) for evaporative mass flux ($\dot{m}_{evp}$) into Eq. (23):

$$-\left[\eta^3\eta_{\xi\xi\xi} - 3\eta^{-1}\eta_\xi - G_1\eta^3(\eta_{\xi\xi}\theta)_\xi - \frac{3}{2}G_1G_2\eta^2\theta_\xi\right]_\xi - \frac{3L_s}{h_0}\left[\eta^2\eta_{\xi\xi\xi} - 3\eta^{-2}\eta_\xi - G_1\eta^2(\eta_{\xi\xi}\theta)_\xi - G_1G_2\eta\theta_\xi\right]_\xi = G_3[\theta - \eta_{\xi\xi} + G_1\theta\eta_{\xi\xi} - \eta^{-3}] \tag{36}$$

where

$$G_1 = \frac{\gamma\Delta T_0}{\sigma_0}, \quad G_2 = \frac{x_0^2}{h_0^2}, \quad G_1 = \frac{3Ca}{\left(\frac{\Pi_0 h_0}{\sigma_0}\right)^2},$$
$$\theta = \frac{\Delta T_0 + \kappa(\eta\eta_{\xi\xi} + \eta^{-2})}{\Delta T_0 + \kappa\eta + \kappa G_1\eta\eta_{\xi\xi}}$$

The differential equation (36) can be also solved by the same method as stated previously. The slip length (L_s) is calculated from Eq. (10). Asymptotic value of slip length (L_{s0}) and critical value of shear rate (γ_c) are obtained using physical properties of pentane such as molecular mass, number density and molecular weight as stated in [16], and the shear rate ($\dot{\gamma}$) is iteratively calculated from the velocity profile.

Fig. 8 shows the thin film thickness profiles with and without consideration of the slip boundary condition, represented by Eqs. (8) and (10), for pentane at vapor temperature of 300 K under the equivalent superheat of 0.01 K. This figure shows that the slip condition tends to increase the length of the thin film and the thermocapillary effect tends to decrease it. As stated previously, the thermocapillary stress resulting from interfacial temperature gradient has an effect of reduction in the length of thin film. On the other hand, slip at the wall reduces the momentum transfer at the wall–fluid interface, and in turn this leads to larger velocity relative to the case of no-slip. Thus, there is less flow resistance in the thin film. As a result, more flow can be provided into the thin film region and consequently the length of the thin film is increased with reduction of flow resistance resulting from slip at wall. The slip length was obtained using thermophysical properties at working temperature by a correlation of Thompson and Troian [20]. The slip length is calculated to be 4.2-nm for pentane and to 5.7-nm for ammonia.

Fig. 9 shows the evaporative mass flux distribution for pentane at two different superheat levels and two different pore sizes, and all cases clearly show increased evaporative mass flux for the case of slip in comparison with no-slip. Note that the slip condition allows more liquid to flow into the thin film region from the bulk liquid because of the reduced viscous drag at the solid–liquid interface. The evaporative heat flow rate is

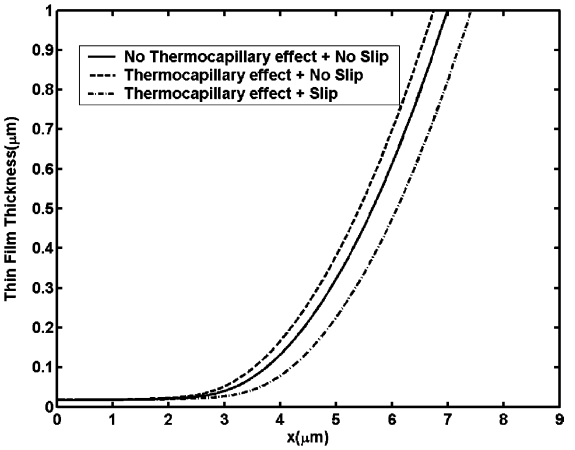

Fig. 8. Dependency of thin film profiles on the thermocapillary effect and on the slip condition for pentane (non-polar) at T_v = 300 K and $T_w - T_v$ = 0.01 K.

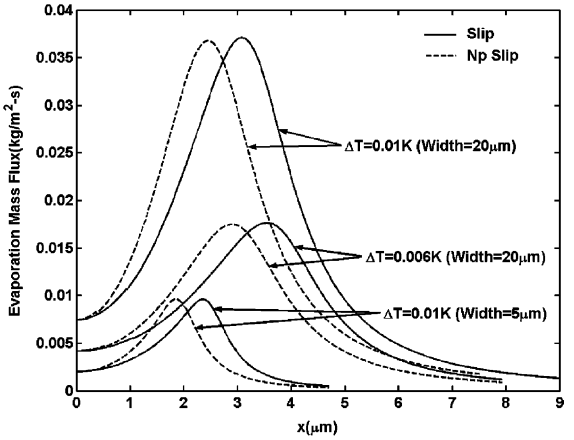

Fig. 9. Evaporative mass flux under slip or no-slip wall conditions at different superheat levels for pentane at T_v = 300 K.

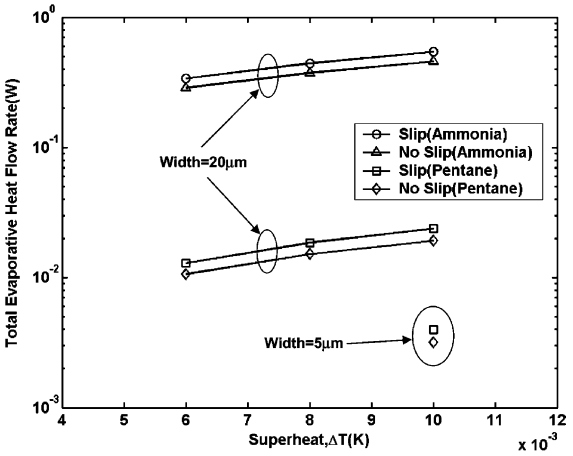

Fig. 10. Total evaporative heat flow rate per unit depth for both slip and no-slip wall conditions at different superheat levels for pentane and ammonia.

determined by multiplying the latent heat of vaporization by the evaporative mass flux. For the superheat of 0.01 K for pentane, the evaporative mass flow rate per unit depth for large slotted pore of 20 μm is 6.59×10^{-8} kg/m s for slip condition and 5.33×10^{-8} W/m for no-slip condition, which presents 24% increase due to the slip condition. For smaller pore of 5 μm in width, the evaporative mass flow rate per unit depth is 1.10×10^{-8} and 8.78×10^{-9} kg/m s for slip and no-slip condition, respectively, which indicates 25% increase due to the slip condition. Considering equivalent cross-sectional area, the area of 16 small pores of 5 μm is equal to that of large pore of 20 μm. Thus, a bundle of 16 small pores could evaporate 1.76×10^{-7} and 1.4×10^{-7} kg/m s for slip and no-slip, respectively, which represents significant increase in evaporative mass flow rate relative to a single large pore.

The total evaporative heat flow rates for the two different sized pores, integrated along the thin film region length with unit width, are shown for both slip and no-slip conditions at different superheat levels for pentane and ammonia in Fig. 10. The slip cases consistently show larger heat flow rates than the no-slip cases for both working fluids and at all superheat levels.

Fig. 11a shows the distribution of the liquid pressure gradients associated with and without the slip boundary condition. The slip at wall reduces the flow resistance and lowers the pressure gradient. Note that the slip effect is more pronounced at higher superheat associated with larger pressure gradients. This trend can be explained by the definition of the slip velocity, Eq. (15), which states that the slip velocity increases with increasing liquid pressure gradient. Fig. 11b shows the distribution of liquid pressure in thin film region. It also confirms that the liquid pressure gradient decreases with the used of the slip condition. Also noted is that slip elongates the thin film region, which is consistent with the observations made from Fig. 8.

To better understand the slip effect on heat and mass transfer, a scaling analysis can be used to identify the parameters controlling the slip length and velocity in the evaporating thin film. First, a characteristic axial velocity, u^*, is defined using the thin film mass flux present at the beginning of the thin film region as

$$u^* = \Gamma_{tr}/\rho_l h_{tr} \tag{37}$$

where the subscript 'tr' refers to conditions at the transition between the bulk meniscus and the thin film. The transition mass flux can be related to the total heat transfer from the thin film according to

$$\Gamma_{tr} h_{fg} \cong k\frac{T_w - T_i}{h_{tr}}\cdot L_{tr} \cong k\frac{T_w - T_v}{h_{tr}}\cdot L_{tr} \tag{38}$$

The transition film length L_{tr} can be scaled using the lubrication form of the x-momentum equation. Ignoring thermocapillary stresses and scaling derivatives in u by $u^* - u_s$ yields

$$\frac{u^* - u_s}{h_{tr}^2} \cong \frac{\Pi_0 - \Pi_{tr}}{L_{tr}}. \tag{39}$$

Eq. (39) is rearranged with respect to L_{tr},

$$L_{tr} \cong \frac{(\Pi_0 - \Pi_{tr})h_{tr}^2}{u^* - u_s} \tag{40}$$

Eq. (40) shows that the transition film length increases as u_s increases. Such a trend was confirmed in Fig. 8. By combining Eqs. (37), (38) and (40) a final scaling for u^* is obtained.

$$u^*\cdot(u^* - u_s) \cong \frac{k}{\rho_l h_{fg}}\frac{T_w - T_v}{h_{tr}^2} h_{tr}^2(\Pi_0 - \Pi_{tr}) \tag{41}$$

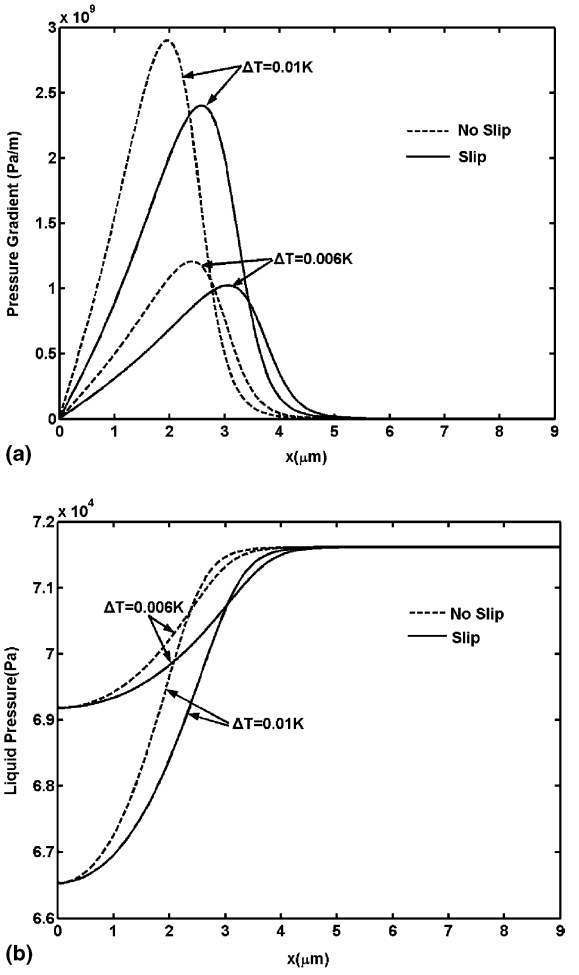

Fig. 11. Liquid pressure profiles in the transition region of pentane at $T_v = 300$ K for different superheat conditions with slip and no-slip wall conditions: (a) liquid pressure gradient calculated; and (b) liquid pressure distribution integrated from (a).

The slip velocity can be scaled as

$$u_s \cong u^* \left(\frac{L_s}{h_{tr}}\right) \tag{42}$$

Thus, the velocity scale, u^*, can be rewritten as

$$u^{*2}\left(1 - \frac{L_s}{h_{tr}}\right) \cong \frac{k}{\rho_l h_{fg}} (T_w - T_v)(\Pi_0 - \Pi_{tr}) \tag{43}$$

$$u^* = \left\{ \frac{k}{\rho_l h_{fg}} \frac{(T_w - T_v)(\Pi_0 - \Pi_{tr})}{(1 - L_s/h_{tr})} \right\}^{1/2} \tag{44}$$

The total heat transfer from the thin film can then be scaled as

$$Q \cong \Gamma_{tr} h_{lv} \tag{45}$$

$$Q = \left\{ \frac{k}{\rho_l h_{fg}} \frac{(T_w - T_v)(\Pi_0 - \Pi_{tr})}{(1 - L_s/h_{tr})} \right\}^{1/2} \rho_l h_{fg} h_{tr} \tag{46}$$

Eq. (46) describes that for a given superheat condition $(T_w - T_v)$ and $(\Pi_0 - \Pi_{tr})$, a larger slip length yields an increased heat transport. This result was also confirmed in Fig. 10.

4. Conclusion

A mathematical formulation has been developed to investigate polarity effects of the disjoining pressure on the fluid flow and heat/mass transfer processes occurring in an evaporating capillary pore with radius of 10-μm incorporating thermocapillary stress. The effect of the slip velocity condition at wall has been separately examined for non-polar pentane and weakly polar ammonia in a two-dimensional slotted pore.

Fundamental findings include the following:

(1) Under the same thermal condition, the thin film length is extended for consideration of a polar form of the disjoining pressure.
(2) The liquid polarity reduces the evaporative heat transfer fluxes due to the stronger van der Waals forces of polar liquid, while the total heat transfer rate reduction is substantially less pronounced.
(3) Consideration of slip at the wall tends to elongate the transition film, thereby counteracting the thermocapillary action of reducing the film length and possibly delaying the onset of thermocapillary driven instabilities.
(4) Slip yields lower pressure gradient in the transition film region, thus enhancing the evaporative mass flux. These slip effects becomes more pronounced at higher superheat conditions.
(5) Non-dimensional analysis of related terms also confirmed the computational findings for the slip effect on the transition film.

Acknowledgment

The authors acknowledge that the current research has been partially sponsored by the NASA-Fluid Physics Research Program Grant No. NAG 3-2712. The presented technical contents are not necessarily the representative views of NASA.

References

[1] H.B. Ma, G.P. Peterson, D.M. Pratt, Disjoining pressure effect on the wetting characteristics in a capillary tube, Microscale Thermophys. Eng. 26 (1998) 157–162.

[2] R. Stephan, J. Hammer, A new model for nucleate boiling heat transfer, Warme Stoffubertrag. 30 (1994) 119–125.
[3] M. Potash Jr., P.C. Wayner Jr., Evaporative from a two-dimensional extended meniscus, Int. J. Heat Mass Transfer 15 (1972) 1851–1863.
[4] B.V. Derjagin, S.V. Nerpin, N.V. Churev, Effect of film transfer upon evaporation of liquids from capillaries, RILEM Bull. 29 (1965) 93–98.
[5] P.C. Wayner Jr., Y.K. Kao, L.V. LaCroix, The interline heat transfer coefficient of an evaporating wetting film, Int. J. Heat Mass Transfer 19 (1976) 487–492.
[6] S. Moosman, G.M. Homsy, Evaporating meniscus of wetting fluids, J. Colloid Interface Sci. 73 (1) (1980) 212–223.
[7] A. Mirzamoghadam, I. Catton, A physical model of the evaporating meniscus, ASME J. Heat Transfer 110 (1988) 201–207.
[8] P.C. Stephan, C.A. Busse, Analysis of the heat transfer coefficient of grooved heat pipe evaporator walls, Int. J. Heat Mass Transfer 35 (1992) 383–391.
[9] L.W. Swanson, G.C. Herdt, Model of the evaporating meniscus in a capillary tube, ASME J. Heat Transfer 114 (1992) 434–441.
[10] K.P. Hallinan, H.C. Chebaro, S.J. Kim, W.S. Chang, Evaporation from an extended meniscus for nonisothermal interfacial conditions, J. Thermophys. Heat Transfer 8 (4) (1994) 709–716.
[11] K. Park, K.J. Noh, K.S. Lee, Transport phenomena in the thin-film region of a micro-channel, Int. J. Heat Mass Transfer 46 (2003) 2381–2388.
[12] R.H. Logan, General Chemistry, 1996. Available from: <http://members.aol.com/profchm/index.html>.
[13] A. Carpi, Atomic Bonding in Introduction to Science in Society, 1998. Available from: <http://web.jjay.cuny.edu/~acarpi/NSC/index.htm>.
[14] J.N. Israelachvili, Intermolecular & Surface Forces, Academic Press, New York, 1992.
[15] W. Qu, T. Ma, Effects of the polarity of working fluids on vapor-liquid flow and heat transfer characteristics in a capillary, Microscale Thermophys. Eng. 6 (2002) 175–190.
[16] M. Gad-el-Hak, Flow physics in MEMS, Mec. Ind. 2 (2001) 313–341.
[17] E. Ruckenstein, C.S. Dunn, Slip velocity during wetting of solids, J. Colloid Interface Sci. 59 (1) (1977) 135–138.
[18] P. Neogi, C.A. Miller, Spreading kinetics of a drop on a smooth solid surface, J. Colloid Interface Sci. 86 (2) (1982) 525–538.
[19] E. Ruckenstein, P. Rajora, On the no-slip boundary condition of hydrodynamics, J. Colloid Interface Sci. 96 (2) (1983) 488–491.
[20] P.A. Thompson, S.M. Troian, A general boundary condition for liquid flow at solid surfaces, Nature 389 (1997) 360–362.
[21] C.H. Choi, K.J.A. Westin, K.S. Breuer, To slip or not to slip water flows in hydrophilic and hydrophobic microchannels, in: Proceedings of IMECE 2002, ASME International Mechanical Engineering Congress & Exposition, November 17–22, 2002, New Orleans, LO, IMECE2002-33707.
[22] D.C. Tretheway, C.D. Meinhart, Apparent fluid slip at hydrophobic microchannel walls, Phys. Fluids 14 (3) (2002) L9–L12.
[23] S. DasGupta, J.A. Schonberg, P.C. Wayner Jr., Investigation of an evaporating extended meniscus based on the augmented Young–Lapalce equation, ASME J. Heat Transfer 115 (1993) 201–208.
[24] D.M. Pratt, J.R. Brown, K.P. Hallinan, Thermocapillary effects on the stability of a heated, curved meniscus, ASME J. Heat Transfer 120 (1998) 220–226.
[25] B.V. Derjaguin, Z.M. Zorin, Optical study of the adsorption and surface condensation of vapours in the vicinity of saturation on smooth surface, in: J.H. Schlman (Ed.), Proc. 2nd Int. Conf. Surface Activity, vol. 2, Butterwoods, London, 1957, pp. 145–152.
[26] F.W. Holm, S.P. Goplen, Heat transfer in the meniscus thin film transition region, ASME J. Heat Transfer 101 (1979) 543–547.
[27] C.L.M.H. Navier, Momentum equation with frictional resistance, Memoirs l'Acad. Royale Sci. l'Instit. Fr. 1 (1823) 414–416.
[28] R.W. Schrage, A Theoretical Study of Interphase Mass Transfer, Columbia University Press, New York, 1953.
[29] P.C. Wayner Jr., The effect of interfacial mass transport on flow in thin liquid films, Colloids Surf. 52 (1991) 71–84.
[30] NIST Chemistry WebBook, NIST Standard Reference Database Number 69, March 2003 Release. Available from: <http://webbook.nist.gov/chemistry/>.